JOURNAL OF GEOPHYSICAL RESEARCH, VOL. 103, NO. C13, PAGES 30,641-30,660, DECEMBER 15, 1998

A model of the circulation on the outer Scotian Shelf with open boundary conditions inferred by data assimilation

Keith R. Thompson and David A. Griffin[1]

Department of Oceanography, Dalhousie University, Halifax, Nova Scotia, Canada

Abstract. The circulation on Western Bank is described using data collected in spring 1991 and 1992 as part of an interdisciplinary study of the early life history of Atlantic cod (*Gadus morhua*). The mean circulation over the crest of the bank is weak, of the order of a few centimeters per second, and is flanked to the south and west by an anticyclonic flow with a speed of about 10 cm s^{-1}. A thermal wind calculation shows the mean circulation is due primarily to horizontal variations in the density field. The M_2 tidal constituent is dominant and reaches speeds of about 20 cm s^{-1}. The tidal residuals have a standard deviation of about 10 cm s^{-1} and characteristic time and length scales of several days and tens of kilometers, respectively. In order to help collect and interpret biological data from Western Bank, we developed a hydrodynamic model of the near-surface flow that could be used operationally. The model is based on a decomposition of the flow into components driven by (1) local wind stress, (2) horizontal density gradients, and (3) flows through the open boundaries of the model. The wind-driven component is calculated using a simple slab model driven by the observed wind. The other two components are estimated through the assimilation of observed bottom pressures, dynamic heights, and currents into the hydrodynamic model. The hindcast skill of the model is quantified by cross validation and shown to be higher than that of four simple, statistically based schemes.

1. Introduction

The continental shelf off the east coast of Canada is wide and rugged with numerous deep basins and banks (Figure 1). Just beyond the shelf break are the two major western boundary currents of the North Atlantic, the Gulf Stream and Labrador Current, both of which are strongly time dependent. Given this setting, it is perhaps not surprising that the subtidal circulation on the middle and outer shelf of eastern Canada is complex in comparison to other North American shelves. For example, *Fissel and Lemon* [1991] concluded that the horizontal scale of subtidal motions on the Labrador Shelf and Labrador Slope is less than 35 km based on an analysis of current measurements made in summer 1980. We show that similar scales apply to the outer Scotian Shelf. By way of contrast, scales exceeding 500 km have been found for the Pacific northwest and the Mid-Atlantic Bight [e.g., *Allen et al.*, 1983].

In this study we address the problem of how to model circulation on the outer shelf. There are several applications for this kind of work, including the prediction of oil spill and iceberg trajectories, marine search and rescue, and the operation of offshore drilling platforms. Our motivation came from the need to understand the reasons for year-to-year changes in the abundance of cod on the Scotian Shelf. As part of a 4-year interdisciplinary study, our biological colleagues in the Ocean Production Enhancement Network (OPEN) proposed to carry out a field program to determine what was special about the small number of cod that survive the larval stage, a critical period in their early life history. They decided against fixed-grid sampling because of the confounding effect of advection. They decided instead to track a group of larvae and repeatedly sample the survivors, along with their physical and biological environment. This, in turn, required a method of mapping the circulation in near real time to help decide when and where to deploy the biological sampling gear.

Given the recent advances in shelf modeling [e.g., *Davies*, 1991; *Lynch and Werner*, 1991; *Mellor*, 1992], mapping circulation on the outer shelf may appear at first sight to be a straightforward exercise. However, the specification of open boundary conditions is an ongoing problem. Often, the boundary flows of limited-

[1]Now at CSIRO Marine Research, Hobart, Tasmania, Australia.

Copyright 1998 by the American Geophysical Union.

Paper number 98JC01765.
0148-0227/98/98JC-01765$09.00

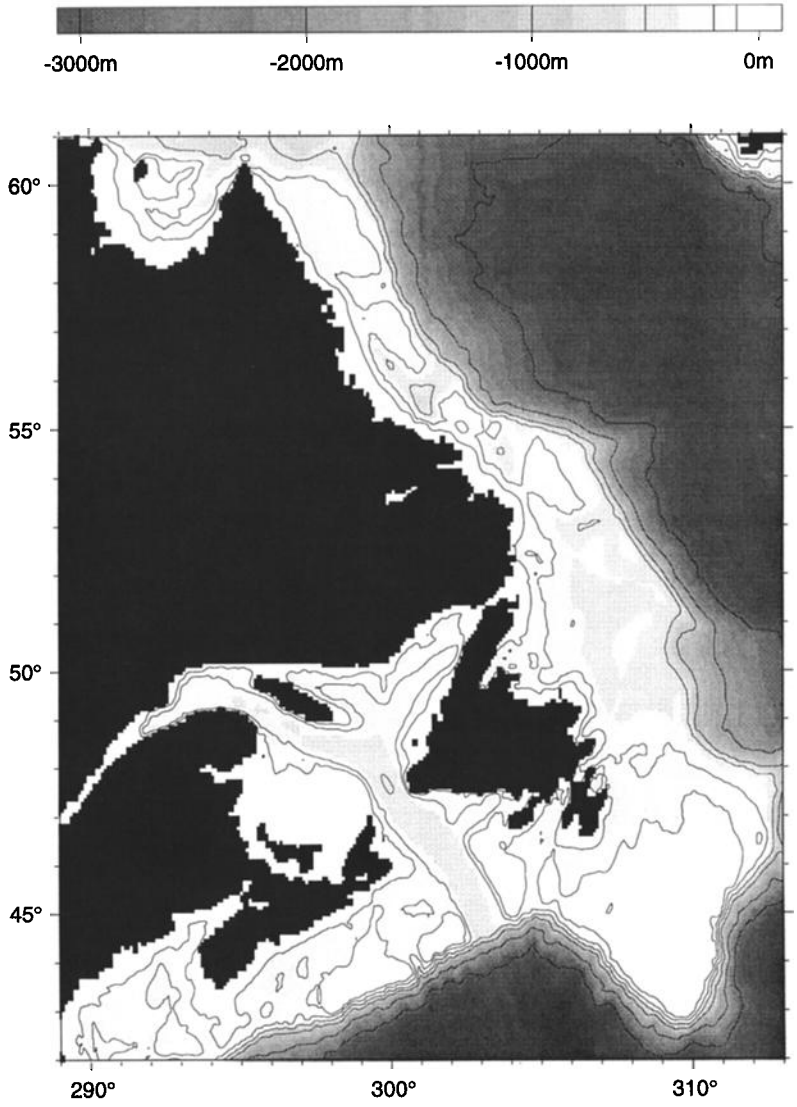

Figure 1. Bathymetry of the east coast of Canada, showing numerous mid-shelf basins and offshore banks. Contours define depths of 100, 200, 500, 1000, 2000, and 3000 m.

area models control the main features of the interior circulation. This has been demonstrated clearly in studies of the circulation over the long, smooth shelves of North and South America that are known to be guides for coastal trapped waves [e.g., *Allen et al.*, 1983]. In practice, it is usually impossible to specify the open boundary conditions based on direct observation and ad hoc schemes must be used to infer them [e.g., *Schwing*, 1992a, b].

Statistical methods such as optimal interpolation [e.g., *Bretherton et al.*, 1976] provide an alternative way of mapping shelf circulation. However, such methods usually require information on the spatial scales of the currents, and such information was not available for our study area. We were also concerned that such scales may depend strongly on frequency (e.g., tides more spatially uniform than subtidal motions) and that the usual assumptions of homogeneity and isotropy may not apply on the outer Scotian Shelf.

In the present study we used a combination of statistical and dynamical modeling in which the unknowns of the circulation model, including its open boundary conditions, are estimated from all available observations. Integrating the model forward in time then gives dynamically consistent maps of the flow. As explained in the appendix the estimation procedure involves systematically adjusting the model unknowns to minimize a cost function that includes a term proportional to the mean square difference between observations and predictions.

The fitting of time-dependent dynamical models to observations is not new. For example, it has been an essential element of meteorological forecasting for decades [e.g., *Daley*, 1991]. In oceanography [e.g., *Bennett*, 1992], assimilation has been an active area of research for about 10 years, driven by the need for operational models of shelf and ocean circulation and ways of interpreting the vast amount of data now provided by satel-

lites. Much of the early oceanographic research was exploratory in nature, with model output assimilated back into the same model in order to test the effectiveness of the assimilation scheme. In recent years there has been a shift toward the assimilation of observations into more realistic ocean models [e.g., *Ghil and Malanotte-Rizzoli*, 1991; *Tziperman, et al.*, 1992; *Marotzke and Wunsch*, 1993]. Our need for a scheme that was capable of assimilating noisy observations in real time forced us to base it on relatively simple dynamics. It was not feasible, given the computer resources and development time available, to base the assimilation scheme on a model as sophisticated as, for example, the Princeton Ocean Model [*Mellor*, 1992]. In retrospect this was probably advantageous because it allowed us to address a number of generic questions that arise when observations are assimilated into any circulation model, simple or sophisticated. They include (1) How does one cope with the relatively small number of observations compared to the large number of unknowns in the circulation model? (2) How does one assess the performance of the assimilation model given that it is "driven" by the observations?

In a companion paper, *Griffin and Thompson* [1996] (hereinafter referred to as GT) describe how the assimilation scheme was used to track a group of cod larvae on Western Bank over a 19-day period in winter 1992. The present study complements GT with a more complete description of the physical oceanography of Western Bank, using data collected in spring 1991 and 1992 (Figure 2). It also provides another assessment of the hindcast skill of the assimilation scheme, this time for spring 1992. This period was characterized by relatively weak winds, compared with the winter period examined by GT. This allowed us to use a simple slab model to predict the wind-driven currents. Many more density profiles were also available for spring, compared with winter 1992. This allowed a cleaner separation of the barotropic and baroclinic components. Finally, this study extends GT by providing more details on the assimilation scheme, its relationship to multiple regression, how prior knowledge about the circulation was introduced and, finally, how hindcast skill was assessed.

In section 2 we summarize the physical oceanography of Western Bank during spring. After presenting

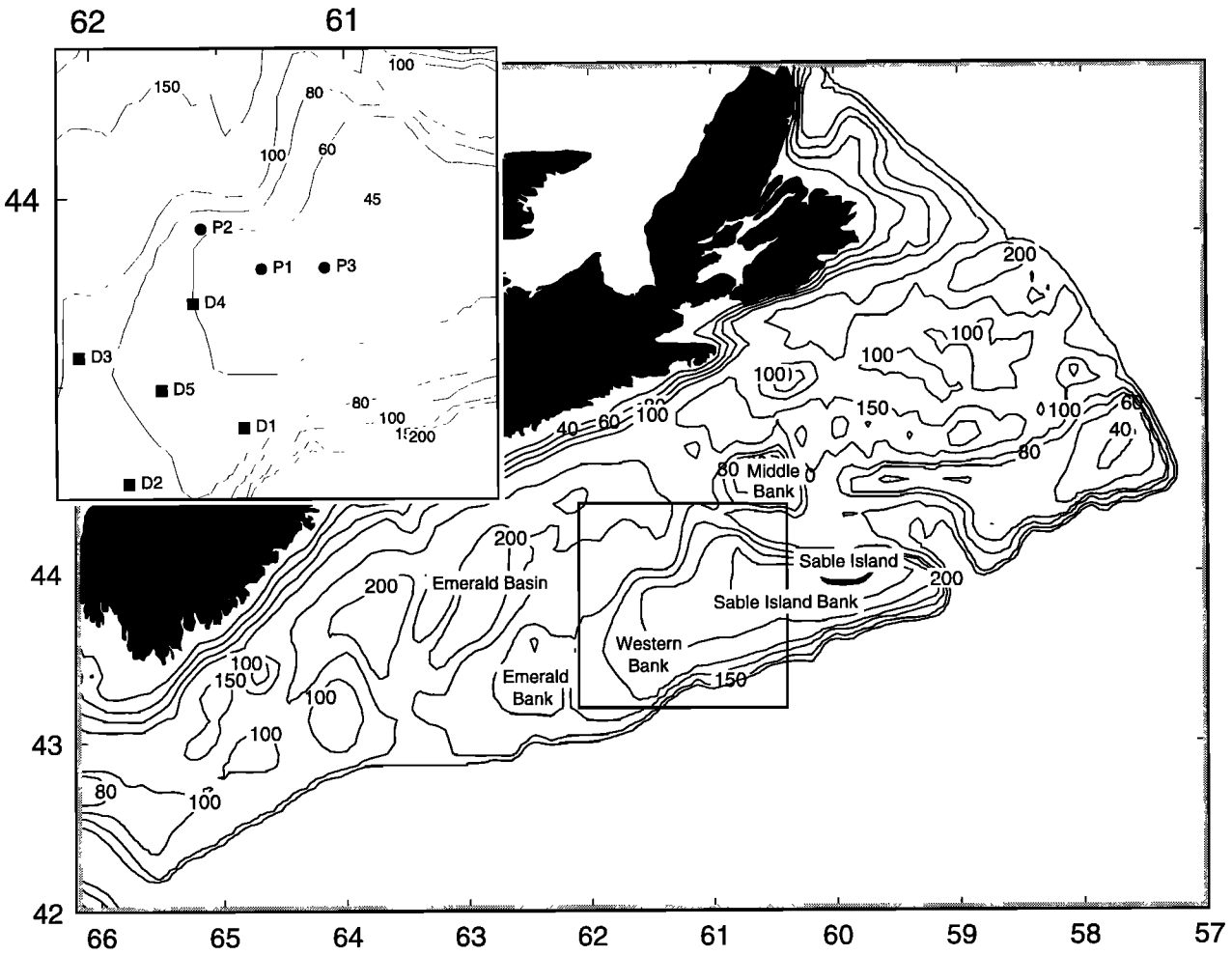

Figure 2. Bathymetry of the Scotian Shelf. Depths are in meters. The inset shows the bathymetry of Western Bank, with squares denoting the positions of the five current moorings (D1-D5) deployed in spring 1991, and dots denoting the positions of three current moorings (P1-P3) deployed in spring 1992. Data from P1-P3 are assimilated into the circulation model.

some basic statistics on the flow, including characteristic length and timescales for the tidal residuals, we argue that an effective limited-area model of the surface flow must include the effect of wind, tides, horizontal density gradients, and open boundary flows. The circulation model and the assimilation scheme are outlined in sections 3 and 4, respectively. In section 5 the method is applied to Western Bank, and in sections 6 and 7 the choice of regularization terms and hindcast skill of the model are discussed. Results are summarized and suggestions made for further work in section 8.

2. Background Physical Oceanography

Mean currents at the seven moorings deployed in spring 1991 and 1992 suggest a near-surface, anticyclonic flow around the south and west flanks of Western Bank with speeds of about 10 cm s^{-1}(Figure 3). The flow over the crest is weak. Repeated hydrographic sections made during winter and spring show warm (temperature $T > 4°C$), salty (salinity $S > 33$ practical salinity units) water wrapped around the south and west flanks of the bank below 70 m [*Griffin and Lochmann*, 1993; *Griffin and Cahill*, 1993]. Similar temperature and salinity distributions are evident at other times of the year based on our analysis of all the hydrographic data collected in the region over the last 70 years. A typical hydrographic section across the bank is shown in Figure 4. Assuming zero flow at the seafloor, the thermal wind relationship implies a northward surface geostrophic flow of 20 cm s^{-1} through the section connecting stations S1 and S7. The speed between S4 and S7 is about 10 cm s^{-1}, similar in magnitude to that observed at D4 and P2 (Figure 3). The same thermal wind calculation implies zero flow over the crest of the bank, consistent with Figure 3, and a generally southwestward flow between S9 and S18. The overall picture that emerges from the density and current data is an anticyclonic, near-surface circulation around Western Bank with speeds of about 10 cm s^{-1}. This picture

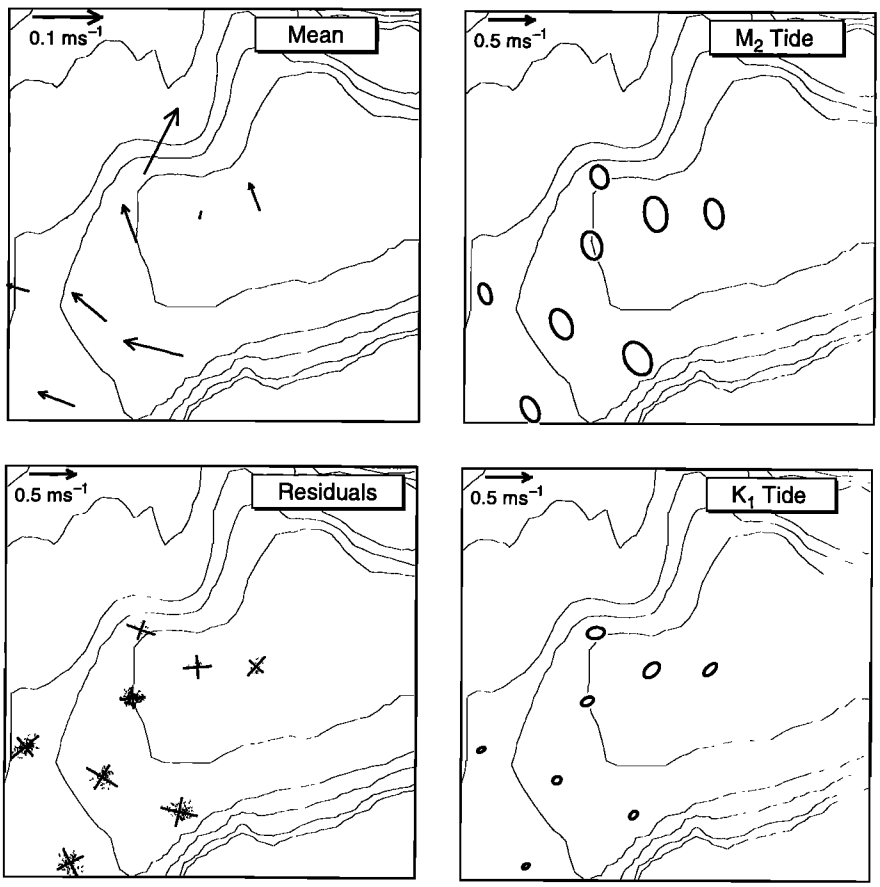

Figure 3. Mean currents, tidal ellipses of the main diurnal and semidiurnal constituents, and scatterplots of tidal residuals at the seven moorings shown in Figure 2. Note the different scale for the mean currents. Each ellipse shows the path of the tip of a tidal current vector as it moves over one tidal cycle. The vector is referenced with respect to the mooring location. The axes for the residual scatterplots are aligned with the principal axes of variation. The lengths of the axes correspond to 2 standard deviations. The currents at moorings D1-D5 (see Figure 2) were measured at 30 m and cover the period 0000 UT on February 26, 1991, to 0000 UT on April 13, 1991. The currents at moorings P2-P3 and P1 were at 20 and 14 m, respectively, and cover the period 1600 UT on April 20, 1992, to 0500 UT on May 5, 1992.

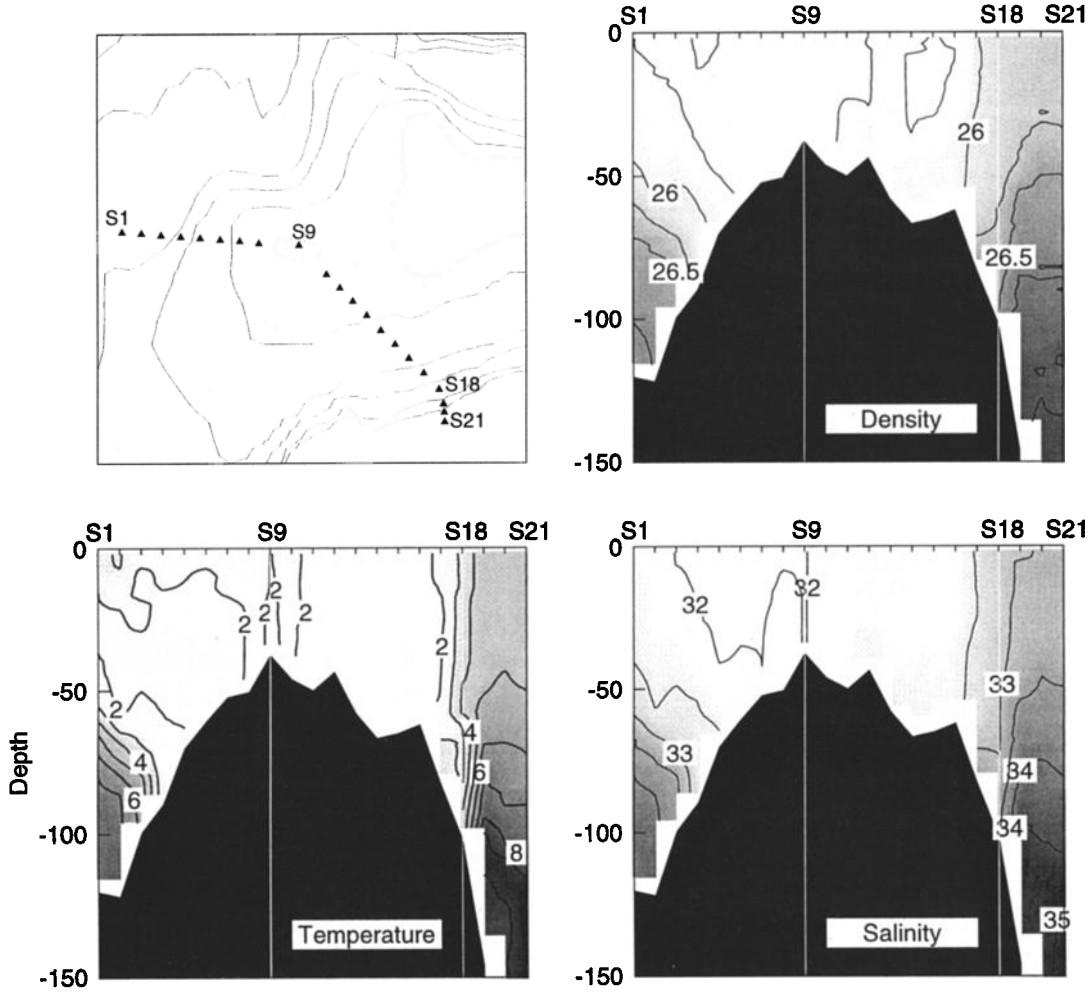

Figure 4. Water density, temperature, and salinity on a section running from (top left) northwest to southeast across Western Bank during the spring 1992 cruise. The locations of the 21 stations (S1 to S21) are marked by triangles. The timing of the stations is given in Figure 7.

is consistent with a more detailed two-dimensional diagnostic calculation based on all density profiles collected in spring 1991 and 1992 [*Dowd and Thompson*, 1996].

The M_2 currents reach speeds of 20 cm s^{-1}. The strongest diurnal constituent is K_1, and it reaches speeds of about 10 cm s^{-1}. The map of tidal streams for K_1 is simpler than M_2. It is more closely related to water depth, with the strongest currents in shallow water (Figure 3).

Tidal residuals were obtained in the standard way by subtracting tidal predictions from each observed current record. For moorings D1-D5 the following constituents were removed: K_1, O_1, OO_1, $2Q_1$, Q_1 and M_2, S_2, N_2, η_2, L_2, ϵ_2, μ_2, and the shallow water constituent M_4. From the shorter records of P1-P3 we removed K_1, O_1, M_2 and S_2.

The tidal residuals are approximately isotropic at all seven moorings, with mean standard deviations between 6 and 8 cm s^{-1} (Figure 3). Most of the energy is in the form of clockwise motions with periods longer than 2 days (Figure 5). There are near-inertial peaks in the rotary spectra at moorings D2, D3, and D5, but they are shifted to frequencies below f by about 0.5×10^{-5} s^{-1} at D2 and D5. We speculate this shift may be due to a change in the effective inertial frequency from f to $f + \bar{\zeta}/2$ [e.g., *D'Asaro*, 1995, and references therein], where $\bar{\zeta}$ is the vorticity of the mean flow around Western Bank. Assuming solid body rotation with a tangential velocity of 10 cm s^{-1} at a radius of 50 km, the approximate distance of D5 from the crest of the bank, we predict a frequency shift of $\bar{\zeta}/2 = -0.2 \times 10^{-5}$ s^{-1}, which is the same order of magnitude as that observed.

To estimate the spatial scale of the tidal residuals, we have, for each pair of moorings with overlapping data records, resolved the flows into longitudinal and transverse components and calculated their cross correlation. The longitudinal-longitudinal correlations ρ_{ll} drop from about 0.8 at 20 km separation to about 0.3 at 60 km (Figure 6). The transverse-transverse correlations ρ_{tt} drop more rapidly with mooring separation. The longitudinal-transverse correlations ρ_{lt} are generally not significantly different from zero at any separation.

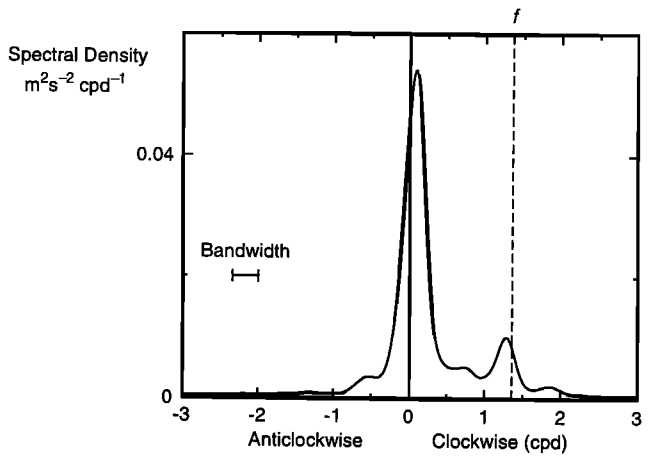

Figure 5. Rotary spectral density of tidal residuals at mooring D5. The inertial frequency is marked by the dashed line. The degrees of freedom for the spectral estimates are 37.1, and the bandwidth is 0.34 cpd.

Although ρ_{ll} and ρ_{tt} are small at 60 km separation, they are significantly different from zero. These correlations may also be of practical significance. To see this, assume the tidal residuals at moorings i and j are the sum of a large-scale common signal C and a small-scale component ϵ_i, ϵ_j:

$$\begin{aligned} u_i &= C + \epsilon_i, \\ u_j &= C + \epsilon_j \end{aligned}$$

where C, ϵ_i, and ϵ_j are uncorrelated and $\mathrm{Var}(\epsilon_i) = \mathrm{Var}(\epsilon_j)$. It is straightforward to show that if the correlation between u_i and u_j is ρ, the correlation between either u and C is $\sqrt{\rho}$. Thus the observed correlation of $\rho = 0.3$ between the most widely separated moorings can be interpreted as a correlation of $\sqrt{\rho} \approx 0.5$ between the currents and a large-scale signal; that is, 30% of the current variance may be due to C.

To test if local wind forcing is the cause of the correlation between current meters, the effect of Sable Island wind stress was removed from each current record using complex regression [e.g., *Brillinger*, 1981] and the correlations were recalculated. The wind stress was lagged to maximize its correlation with the currents. Overall, the current correlations were reduced but their overall dependence on separation remained unchanged (Figure 6). Specifically, ρ_{ll} and ρ_{tt} dropped from about 0.3 to 0.2 at 60 km, suggesting that part, but not all, of the large-scale signal is due to the wind.

To estimate a characteristic length scale for the tidal residuals, we first note that several features of the correlation-separation plots are consistent with the two-point velocity correlation structure predicted by the theory of isotropic, homogeneous turbulence [e.g., *Daley*, 1991]. To illustrate, let

$$\rho_{\psi\psi}(r) = (1 + r/L)\exp(-r/L)$$

define the spatial autocorrelation of the stream function of a nondivergent, random flow field with characteristic length scale L. The correlation of the velocity components at two locations separated by distance r is then [e.g., *Daley*, 1991]

$$\begin{aligned} \rho_{ll} &= \exp(-r/L), \\ \rho_{tt} &= (1 - r/L)\exp(-r/L), \\ \rho_{lt} &= 0. \end{aligned} \tag{1}$$

As shown in Figure 6, $L = 45$ km gives a reasonable fit to the residual correlations, including the slower decay of ρ_{ll} with separation compared with ρ_{tt}, and the near-zero values of ρ_{lt}.

From the above physical description we conclude that an effective model of the circulation on Western Bank must include the effect of wind, tides, and horizontal density gradients. The model must also capture the small scale (order 50 km) motions with a timescale of days. In the following sections we describe our development of a limited-area model of the circulation on Western Bank and the use of data assimilation to infer its open boundary conditions.

3. Dynamical Model

The dynamical model is based on the following linearized horizontal momentum and continuity equations [e.g., *Csanady*, 1982, section 1.9]:

$$\frac{\partial \mathbf{u}}{\partial t} + \mathbf{f} \times \mathbf{u} = -g\nabla\eta - \frac{g}{\rho_0}\int_z^0 \nabla\rho dz + \frac{\partial}{\partial z}\left(\mu\frac{\partial \mathbf{u}}{\partial z}\right), \tag{2}$$

$$\nabla \cdot \mathbf{u} + \frac{\partial w}{\partial z} = 0. \tag{3}$$

The neglect of the nonlinear advection terms is reasonable for Western Bank because, as shown in section 2, the Rossby number for the mean flow, $\overline{\zeta}/f$, is about 0.1. A similar value applies to tidal motions (Figure 3). In addition to standard kinematic boundary conditions at the seasurface and seafloor, we take

$$\mu\frac{\partial \mathbf{u}}{\partial z} = \begin{cases} \tau & z = 0 \\ k\mathbf{u} & z = -h \end{cases} \tag{4}$$

where τ is the kinematic wind stress vector and k is a bottom friction coefficient. (GT discuss the use of a nonlinear bottom stress parameterization.) The lateral boundary conditions are described later in this section.

The circulation is forced by wind stress, horizontal density gradients, and flows through the open boundaries of the model domain. Given that the response to each of these forcings is linear, the near-surface flow can be decomposed as follows:

$$\mathbf{u} = \mathbf{u}_w + \mathbf{u}_d + \mathbf{u}_b \tag{5}$$

where subscripts w, d, and b denote wind, density, and boundary-driven flow components, respectively.

Wind-driven flow $\mathbf{u}_w$. This component satisfies (2)-(4) with $\nabla\rho$ set to zero. The model domain is about

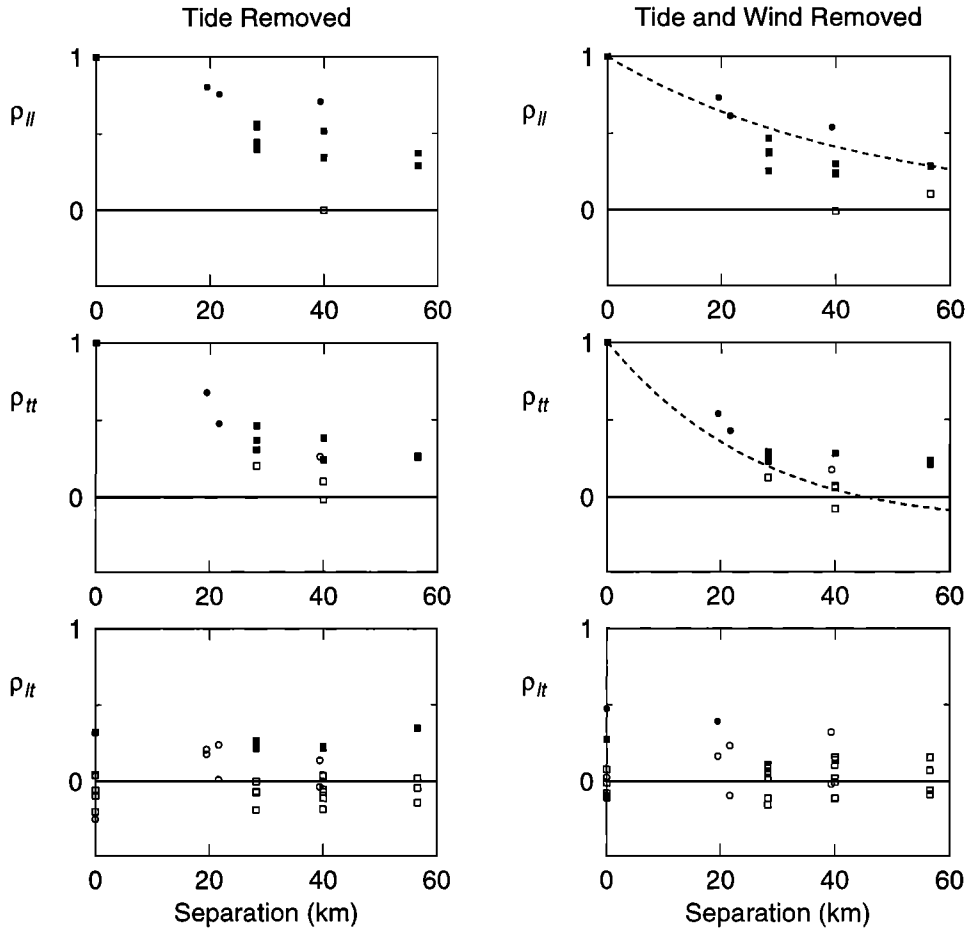

Figure 6. Current correlations as a function of mooring separation for (left) tidal residuals and (right) tidal residuals after removal of the effect of local wind by regression. For each pair of moorings the flows were resolved along the line connecting the moorings (the longitudinal components u_l) and perpendicular to this line (the transverse components u_t). The correlation was then estimated for the longitudinal components ρ_{ll}, the transverse components ρ_{tt}, and the longitudinal and transverse components ρ_{lt}. Solid symbols denote correlations that are different from zero at the 1% significance level. Allowance was made for serial correlation. Squares refer to D1-D5 pairs, and circles denote P1-P3 pairs. Start and end times of the records are given in the Figure 3 caption. The dashed lines are theoretical correlation functions, as defined in the text, with a length scale of 45 km.

100 km square, and so the wind stress may be assumed spatially uniform. The winds were fairly light during the spring 1992 cruise, with stress magnitudes always less than 0.4 Pa. This implies that the thickness of the turbulent surface Ekman layer, estimated using the empirical expression $u_*/10f$ [e.g., *Csanady*, 1982], was always less than the minimum water depth of 45 m. It is thus reasonable to assume the locally forced, wind-driven flow did not "feel the bottom" and to model it with a slab model [*Pollard and Millard*, 1970]:

$$\frac{\partial \mathbf{u}_w}{\partial t} + \mathbf{f} \times \mathbf{u}_w = \frac{\tau}{h_w} - k_I \mathbf{u}_w \qquad (6)$$

where h_w is the thickness of the slab and k_I is an interfacial friction coefficient. The integration of this equation is straightforward, and $\mathbf{u}_w$ can be considered known once h_w, k_I, and τ are specified. We chose $k_I = 0.33 \times 10^{-4}$ s^{-1} and $h_w = 30$ m based on the frequency-dependent transfer functions of observed currents on local wind stress.

Density-driven flow $\mathbf{u}_d$. First note that an equation for the temporal evolution of the density field has not been included in the set of governing equations. Our approach is to diagnose $\mathbf{u}_d$, the density-driven surface flow, from observed density profiles using (2)-(4) with τ set to zero.

Repeated sections made across Western Bank show the main features of the density field and, in particular, the sloping isopycnals below 70 m (Figure 4), do not change significantly on timescales of days [*Griffin and Lochmann*, 1993; *Griffin and Cahill*, 1993]. We have therefore dropped the time-dependent term from (2). Given the present focus on near-surface flow and the fact that the thickness of the bottom Ekman layer is much less than the minimum water depth, it is reasonable to assume $\mathbf{u}_d$ is in geostrophic balance:

$$\mathbf{f} \times \mathbf{u}_d = -g\nabla\eta_d \tag{7}$$

where η_d denotes dynamic height. Thus the problem of estimating $\mathbf{u}_d$ is reduced to the simpler problem of estimating η_d.

Hydrographic sections across Western Bank suggest the density field in spring has adjusted such that bottom density is approximately constant along isobaths. This is evident, for example, in Figure 4 where the 26 and 26.5 density contours can be seen intersecting the bottom at about 75 and 95 m, respectively, on both sides of the bank. If bottom density is constant along isobaths and the bottom geostrophic flow is zero, the following expression [*Helland-Hansen*, 1934; *Csanady*, 1979] can be used to calculate η_d directly from the vertical density profiles:

$$\eta_d = -\frac{1}{\rho_0}\left[\int_{-h}^{0} \rho dz + \int_{-H}^{-h} \tilde{\rho}(h')dh'\right] \tag{8}$$

where H is a deep reference level and $\tilde{\rho}(h)$ is the bottom density. Equation (8) follows from vertical integration of the thermal wind relationship (for discussion and references to earlier work, see *Sheng and Thompson* [1996]). We estimated $\tilde{\rho}$ by averaging the observed bottom densities along isobaths.

Boundary-driven flow $\mathbf{u}_b$. This component satisfies (2)-(4) with both τ and $\nabla\rho$ set to zero. The flow is forced by flows through the open boundaries of the model and includes, for example, the effect of tides, bathymetric scattering of remotely forced shelf waves, and warm core rings interacting with the outer shelf through along-shelf pressure gradients. This component is used to model the tides and the small-scale motions described in section 2. It also allows us to relax the assumption of zero bottom geostrophic flow used in the calculation of $\mathbf{u}_d$. Depth averaging (2) and (3) gives

$$\frac{\partial \mathbf{u}_b}{\partial t} + \mathbf{f} \times \mathbf{u}_b = -g\nabla\eta_b - \frac{\lambda}{h}\mathbf{u}_b, \tag{9}$$

$$\frac{\partial \eta_b}{\partial t} + \nabla \cdot (\mathbf{u}_b h) = 0. \tag{10}$$

Note bottom stress has been parameterized in terms of the depth-mean flow. This is reasonable if the thickness of the bottom Ekman layer is much less than the water depth [e.g., *Csanady*, 1982].

Equations (9) and (10) have been used for many years in the study of tides and surges on continental shelves. Their discretization is straightforward [e.g., *Heaps*, 1972]. At the lateral boundaries we use radiation conditions to ensure long surface gravity waves leave the model domain with minimal reflection (see GT for details). The radiation is about a normal velocity inferred by data assimilation (section 4).

4. Assimilation Scheme

The wind-driven component of flow is readily predicted from the observed wind using the slab model. The remaining flow components require specification of the dynamic height field and normal flows across open boundaries. To limit the number of parameters required for their specification, both the dynamic height field and the boundary flows are expressed as linear combinations of spatial structure functions ϕ_s with time-varying amplitudes α_s. For example, the dynamic height field is expanded as follows:

$$\eta_d = \sum_s \alpha_s(t)\phi_s(x, y). \tag{11}$$

The amplitudes of the structure functions are allowed to evolve slowly through time according to

$$\alpha_s(t) = d_{1s} + d_{2s}t. \tag{12}$$

Thus the problem of estimating the density-driven component of surface flow is reduced to the problem of estimating the d_{1s} and d_{2s}.

A similar approach is used to specify the normal boundary flows required for the integration of (9) and (10). Consider, for example, the transport through a north-south oriented open boundary. It is expressed in a form that parallels (11):

$$uh = \sum_s \alpha_s(t)\phi_s(y) \tag{13}$$

where $h = h(y)$ is the water depth and the structure functions now depend only on the position y along the open boundary. The time-dependent amplitudes are expressed in a form that generalizes (12):

$$\alpha_s(t) = \sum_k b_{ks}\omega_k(t) \tag{14}$$

where $\alpha_s(k\Delta) = b_{ks}$ and $\omega_k(t)$ interpolate $\alpha_s(k\Delta)$ to intermediate times. We took $\Delta = 3$ hours so that the semidiurnal tides could be resolved. Lagrange four-point interpolation [e.g., *Abramowitz and Stegun*, 1965] was used to define $\omega_k(t)$.

The d_{ks} and b_{ks} are estimated by minimizing the following cost function:

$$J = J_{obs} + J_{mod}.$$

J_{obs} is proportional to the mean square difference between observations (currents, dynamics heights, and bottom pressures) and model predictions. Denoting the ith observation by y_i and its model counterpart by $\hat{y}_i$,

$$J_{obs} = \frac{1}{2}\sum_{i=1}^{N}\sum_{j=1}^{N}(y_i - \hat{y}_i)w_{ij}(y_j - \hat{y}_j) \tag{15}$$

where N is the total number of observations and w_{ij} are weights that can be organized in the positive-definite matrix $W = \{w_{ij}\}$. As discussed in the appendix, there are statistical reasons for taking W to be an estimate of Σ^{-1}, where Σ is the $N \times N$ covariance matrix of $y_i - \hat{y}_i$.

J_{mod} depends on the statistical properties of the model flow fields. In the present study we take

$$J_{mod} = J_d + J_b + J_v. \tag{16}$$

These regularization terms are used to penalize certain properties of the model flow fields. (See the appendix

for more details.) The first term, J_d, is proportional to the mean kinetic energy of the density-driven flow:

$$J_d = \frac{1}{2\sigma_d^2} \sum_{ijt} |\mathbf{u}_d^{ijt}|^2 \tag{17}$$

where t is evaluated at the beginning and end of the model integration and i, j are evaluated on a grid of positions covering the model domain. The second term, J_b, is proportional to the mean kinetic energy of the boundary-driven flow:

$$J_b = \frac{1}{2\sigma_b^2} \sum_{ijt} |h_{ij}\mathbf{u}_b^{ijt}|^2 \tag{18}$$

where $t = \Delta, 2\Delta \ldots$ and i, j range over all grid points of the barotropic model. The last regularization term, J_v, depends on the mean square vorticity of the barotropic flow:

$$J_v = \frac{1}{2\sigma_v^2} \sum_{ijt} \zeta_{ijt}^2 \tag{19}$$

where

$$\zeta_{ijt} = u_b^{ijt} - u_b^{(i-1)jt} + v_b^{ijt} - v_b^{i(j-1)t} \tag{20}$$

and $t = \Delta, 2\Delta \ldots$ and i, j range over all interior grid points of the barotropic model. Dividing ζ_{ijt} by the grid spacing gives a finite difference approximation to the relative vorticity of the barotropic flow. We arrived at the above regularization terms after carrying out a large number of assimilation runs. It is convenient to defer further discussion of the choice of these terms and their weights (σ_d, σ_b, and σ_v) to section 6, after we have described a typical run of the assimilation model.

The following standard scheme was used to minimize J: (i) Calculate the wind-driven flow by integrating (6). (ii) Set d_{ks} and b_{ks} to zero. (iii) Calculate the density and boundary-driven responses by integrating (7), (9), and (10). (iv) Add the three flow components and subtract from the observations. Store the model flow fields at the times required to calculate J_{mod}. (v) Calculate

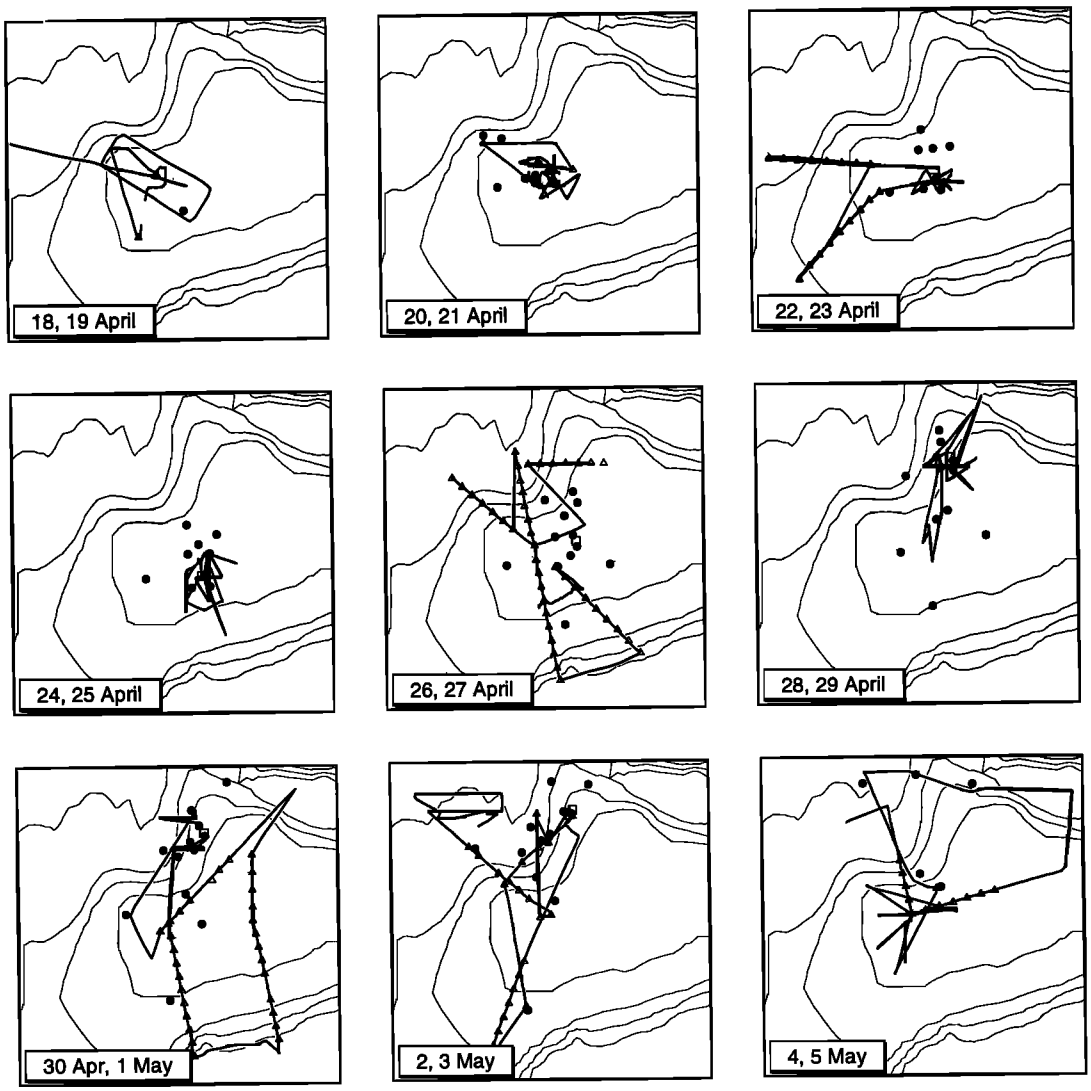

Figure 7. Data availability in 2-day blocks covering the cruise period in spring 1992. The ship's track is shown by the solid line. The triangles mark hydrographic stations along the ship's track. The dots show the positions of the drifters at the beginning of each 2-day block.

the gradient of J with respect to the unknown parameters d_{ks} and b_{ks}. This involves running an adjoint model backward in time, as explained in the appendix. (vi) Update d_{ks} and b_{ks}. We used a linear conjugate gradient descent algorithm [e.g., *Gill et al.*, 1981] that takes advantage of the fact J is a quadratic form. With a slight modification it required only one run of the forward model and one run of the backward model to update the unknowns. (vii) Return to step (*iii*) and repeat the procedure until J effectively reaches its minimum.

Initial conditions for the barotropic model can be treated as unknowns. However, the spin-up time of the barotropic model is about one day, much shorter than a typical integration time. Consequently, the initial conditions have little effect on model fit compared to the boundary conditions. Although initial conditions were treated as unknowns in the early stages of model development, they slowed down significantly the convergence of J. We therefore decided to set them to zero and start the model integration several spin-down times before the assimilation of the first observation.

5. Hindcasting Flow on Western Bank

An application of the assimilation scheme is now described using data collected in spring 1992. A summary of the fieldwork is shown in Figure 7. The research vessel reached Western Bank on April 18 and started to deploy drifters, collect temperature and salinity profiles, and measure velocity with a hull-mounted acoustic Doppler current profiler (ADCP). The drifters were drogued by a 2 × 10 m sail centered at 20 m, and the ADCP had a frequency of 300 kHz. Four current meters were deployed on and around the crest of the bank on April 19. Only three returned good data, and their positions are shown in the inset of Figure 2. The ship then deployed the rest of the drifters and commenced the routine collection of hydrographic and biological data. All drifters and current meters were recovered by May 5. (A full description of the fieldwork and a data inventory are provided by *Griffin and Lochmann* [1992].)

Snapshots of ADCP and drifter velocities at 3-hour intervals covering a typical day are shown in Figure 8. As expected, the motion is mainly tidal, consistent with Figure 3. Note the movement of the ADCP through the survey area and the good agreement between nearby velocity estimates. Typical time series are shown in Figure 9. The tides again dominate as expected. The ADCP record is the least regular due, in part, to the movement of the ship through the spatially varying flow field. Although currents from the mooring and drifter are quite similar at tidal frequencies, differences of order 10 cm s^{-1} are evident at subtidal frequencies.

The spatial structure functions for η_d (see (11)) were taken to be of the form

$$\phi = (x - x_0)^m (y - y_0)^n$$

where (x_0, y_0) defines the center of the model domain. Terms up to and including the fifth power in x and y were used. (This degree was required to resolve the mean gyral circulation around Western Bank.) This results in a total of 21 structure functions. The total number of d_{1s} and d_{2s} to be estimated is therefore $21 \times 2 = 42$.

The barotropic equations were discretized on a 16×16 grid with a spatial resolution of 5 km and a time step of 60 s. The bottom friction coefficient λ was taken to be 6×10^{-4} m s^{-1}. We found that only two inflow structure functions per boundary were required to give reasonable results: $\phi_1 = 1$ and $\phi_2 = (y - y_0)$ in (13). With $\Delta =$ 3 hours and an integration time of 12 days and 15 hours there are 102 unknown b_{ks} for each structure function. With two structure functions for each of the four open boundaries, the total number of b_{ks} to be estimated is $102 \times 8 = 816$.

Two forms for Σ (see (15)) were used. Both are based on the assumption that errors at different times are uncorrelated. The simplest form was a diagonal Σ with elements that depend only on instrument type. This form does not allow for covariance between different $y_i - \hat{y}_i$. Thus two nearby drifters with almost identical trajectories will have the same weight as a pair of widely separated drifters that provide essentially twice as much information about the circulation. The other form for Σ allowed, in a simple way, for covariance between hindcast velocity errors. Specifically, the covariance of eastward velocity errors at two locations, separated by r, was modeled by

$$\sigma_{uu} = \begin{cases} \sigma^2 + \sigma_n^2 & r = 0 \\ \sigma^2 \exp(-r^2/L^2) & r > 0 \end{cases} \tag{21}$$

We assumed $\sigma_{vv} = \sigma_{uu}$ and $\sigma_{uv} = 0$. These covariances are for differences between the observations and model predictions. Such errors may be due, for example, to subgrid-scale shears, Langmuir cells, and convergences associated with localized fronts. There is no reason to expect these motions to be either isotropic or nondivergent. Thus when choosing a simple functional form to approximate the error covariances, we ignored the constraints on ρ_{ll}, ρ_{ll}, and ρ_{lt} that follow from the assumptions of isotropy and nondivergence (see discussion in section 2 with reference to the tidal residuals).

The parameters σ^2, σ_n^2, and L of (21) were estimated by (1) running the assimilation scheme with a diagonal Σ, (2) binning pairs of velocity errors made at the same time and within a certain range $(r \pm \Delta r)$ of each other, (3) calculating the covariance between the binned pairs of velocity errors, and (4) plotting covariance as a function of r.

We found $\sigma^2/(\sigma^2 + \sigma_n^2) = 0.7$ and $L = 5$ km fit the hindcast error covariances reasonably well. This short length scale implies the off-diagonal elements in Σ only come into play when the drifters and ADCP are within a grid cell of each other or the current meter moorings. In practice, such close encounters were quite rare. The result was that hindcasts produced using the two Σ were almost identical.

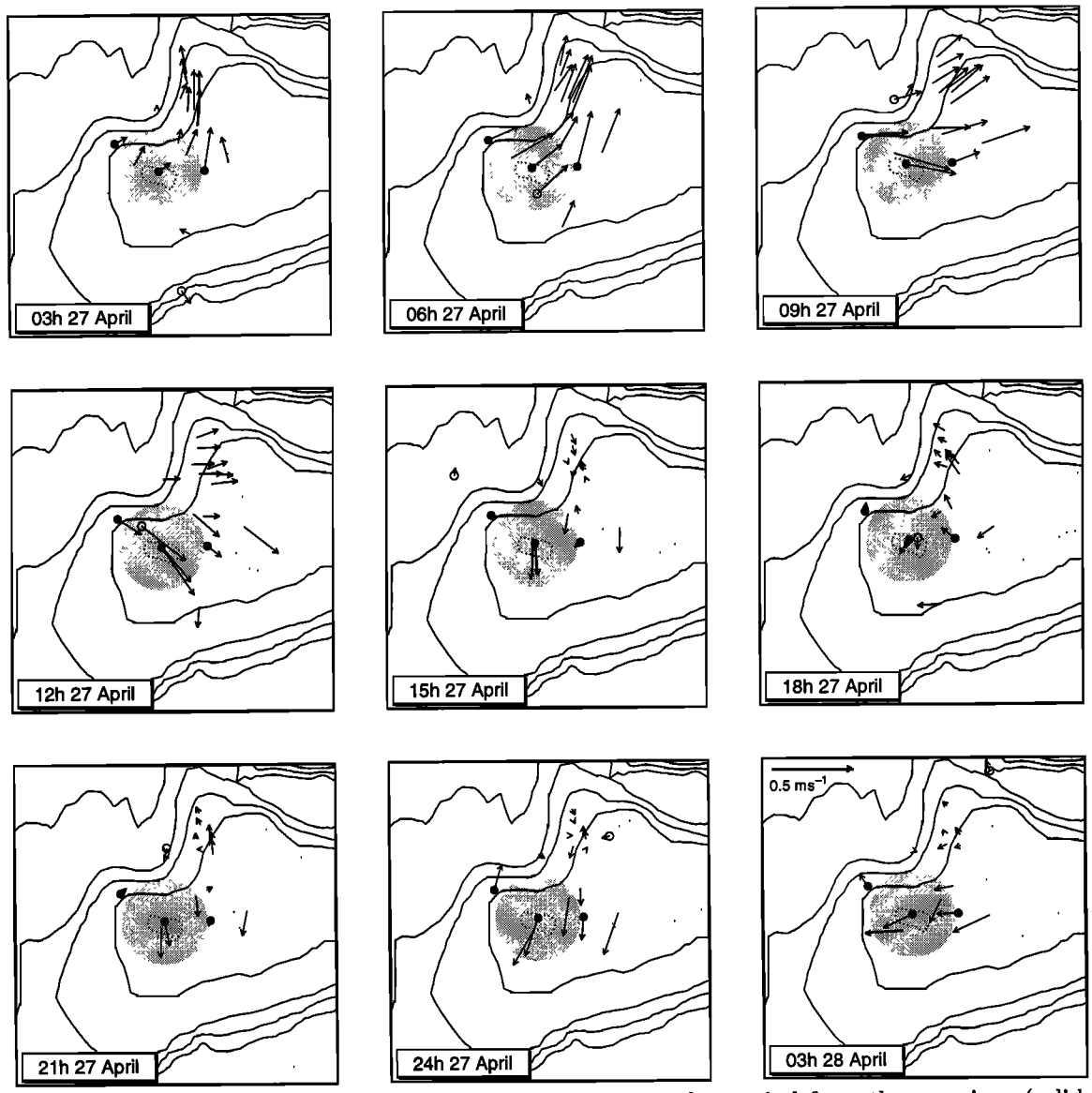

Figure 8. Velocity measurements every 3 hours over a 1 day period from the moorings (solid circles), shipborne acoustic Doppler current profiler (ADCP, open circles) and drifters. The drifter velocities were obtained by time-centered first differencing of the 15-min drifter positions. The other velocities are 15-min averages. The shaded area defines the data void used in the assessment of the performance of the assimilation model.

Best-fitting flow fields are shown in Figure 10 for the same period as the snapshots of observations (Figure 8). Times series of observations and hindcasts are shown in Figure 9. The assimilation model has clearly captured most of the observed variability. The standard deviation of the eastward flow measured by the ADCP is reduced from 13.6 to 3.1 cm s^{-1} upon removal of the model predictions. The corresponding reductions for the drifter and moored current meter records in Figure 9 are 12.2 to 2.7 cm s^{-1} and 13.6 to 4.4 cm s^{-1}, respectively. Averaging across all instruments gives a reduction in observed current variance of about 90% on removal of the model hindcasts.

Tidally filtered flow fields have more spatial structure than the snapshots (compare Figures 10 and 11). This is to be expected because of the tendency of barotropic flow to follow f/h contours more closely with decreasing frequency. The slow backing of the current in the northwest corner of the domain is associated with the density-driven component of flow. The wind-driven component was generally weaker than 5 cm s^{-1}, except for April 26 when it exceeded 10 cm s^{-1}. The result was a relatively uniform subtidal flow pattern for this particular day. Forcing by the southern boundary of the barotropic submodel can be seen on April 24 to 26. A small-scale gyre, forced by barotropic flow across depth contours, is evident on April 27. It subsequently propagated around the bank and left the domain through the northern open boundary.

6. Regularization

We used a combination of numerical experimentation and physical intuition to choose the form of the

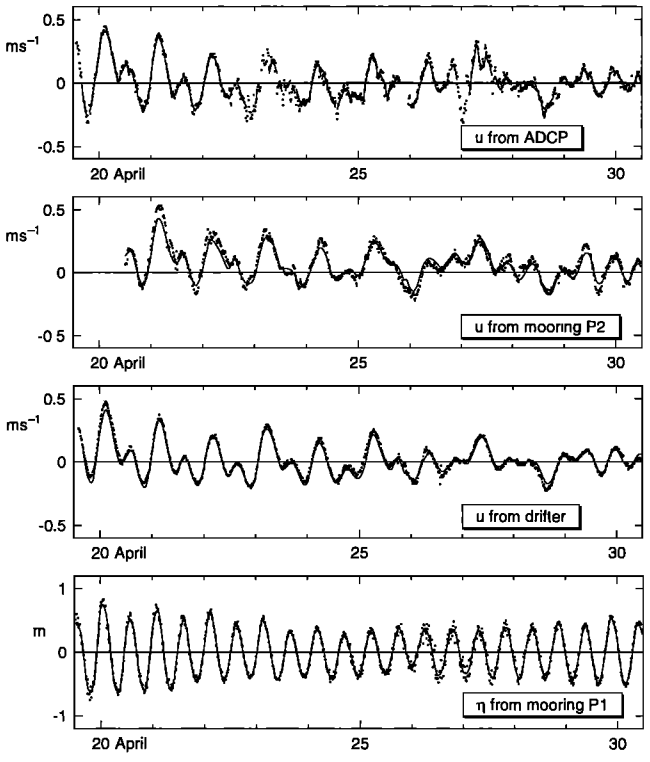

Figure 9. Typical time series, with dots denoting 15-min observations and solid lines denoting hindcasts from the assimilation model. (top to bottom) Eastward flow measured by the shipborne ADCP, where breaks correspond to times when the ADCP was outside the model domain; eastward flow measured at mooring P1; eastward flow measured by a typical drifter; and bottom pressure measured at mooring P1.

regularization terms. To illustrate, in the early stages of model development we used a term proportional to $\sum b_{ks}^2$ to control the overall strength of the boundary-driven flow. The results were unacceptable; strong jets occasionally appeared along the open boundaries and small-scale ($\sim$ 10 km) eddy-like features developed intermittently in the northeast corner of the model domain. Given that this corner is an exit region for long topographic Rossby waves, we interpreted the small-scale features as short, reflected topographic Rossby waves [e.g., *Pedlosky*, 1979]. To suppress such waves, we added the J_v term, defined by (19). It worked well in that the small-scale (high vorticity) features were eliminated. (The open boundaries were now effectively transparent to long, outward propagating topographic Rossby waves.) In addition to J_v, it also proved necessary to append J_b as defined by (18). This term suppressed a domain-wide, irrotational flow pattern that occasionally dominated the barotropic flow component.

An important practical issue is the weight to give the regularization terms. We found the technique of cross validation to be useful. Specifically, we would withhold some observations and then calculate the difference between these observations and the corresponding model hindcasts (henceforth the validation error). Repeating the calculation for a range of σ_d, σ_b, and σ_v, we could find the weighing that minimized the validation error variance. One difficulty with this technique is deciding which data to withhold. After some experimentation we concluded the most effective approach was to withhold data based on recording position. For example, in one validation experiment all data collected within 17 km of the central mooring P1 were withheld. (This radius is just small enough to exclude the other two moorings as shown in Figure 8.) In effect, we created an artificial "data void" around P1 and assessed the ability of the assimilation model to recover the withheld data. To illustrate, we now describe one set of numerical experiments designed to fix σ_b and σ_v. Given the large number of runs to be performed, the results discussed in the rest of this section were obtained using a slightly coarser grid resolution of 7 km. To simplify the discussion, σ_b and σ_v are taken to covary with the single parameter γ as follows:

$$\begin{aligned} \sigma_b &= 4/3\gamma, \\ \sigma_v &= 1/\gamma. \end{aligned} \tag{22}$$

Thus large values of γ correspond to small values of σ_v and σ_b and hence strong penalization of kinetic energy and mean square vorticity.

The plot of validation error variance against γ has a well-defined minimum (Figure 12). The optimal value of σ_b is about 5 cm s^{-1}, and the optimal σ_v implies a root-mean-square barotropic vorticity of about $f/20$. Both values are physically reasonable and consistent with current and vorticity variances estimated a posteriori from the hindcast flow fields. Figure 12 (bottom) shows hindcast error variance at P2 and P3, the two moorings that provided data for assimilation. As expected, weaker penalization (smaller γ) always results in smaller error variance because the model has more flexibility to fit the observations. However, comparison of Figures 12, top and bottom, leads us to conclude that the model is probably overfitting the assimilated data when γ is less than about 0.3.

7. Assessing Hindcast Skill

Cross validation was also used to compare the hindcast skill of the assimilation model against that of several simple statistical schemes. Specifically, the model was used to hindcast the flow at P1 after assimilating only those observations recorded more than 17 km from it (i.e., outside the data void shown in Figure 8). To put the model fit into perspective, the flow at P1 was also hindcast using (1) the observed flow at P2; (2) the observed flow at P3; (3) the average of the observed flows at P2 and P3; and (4) an average of all current observations outside the data void, weighted by a factor that varied as r^{-3}, where r is distance from P1. We first discuss the errors in the mean, followed by errors at tidal periods, and then periods of several days.

The assimilation model recovers the mean flow at P1 with a validation error of less than 2 cm s^{-1} (Table 1). The best statistical hindcast of the mean is the current observed at P3, although the error exceeds 5 cm s^{-1}.

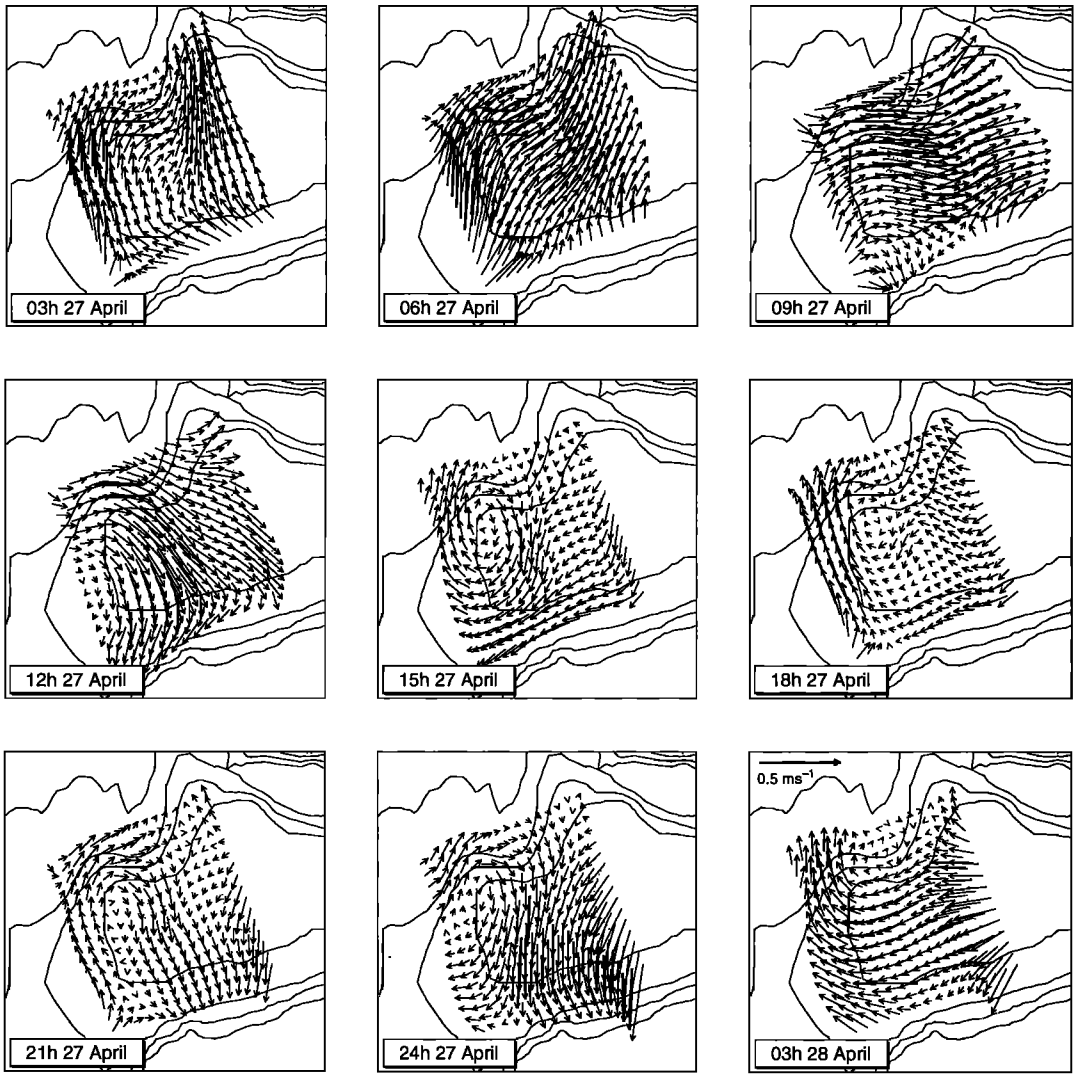

Figure 10. Velocity fields from the assimilation model every 3 hours over a 1-day period. Times are the same as Figure 8. Note, however, that these flow fields are based on data assimilated over the whole observation period, not just April 27, 1992.

The least successful of the statistical hindcasts of the mean is the observed current at P2. The magnitude of its error exceeds 10 cm s^{-1}.

The variance of the observed currents at P1 is 403 cm^2 s^{-2} (Table 1). The variance of the assimilation model errors at P1 is 30 cm^2 s^{-2}. This is much lower than the error variances of all the statistical hindcasts, the most effective of which is the weighted mean of all assimilated observations (59 cm^2 s^{-2}, Table 1). The least successful of the statistical hindcasts is the flow at P2, with an error variance that is more than quadruple that of the assimilation model.

The validation errors have been decomposed into tidal and residual components (Table 1). The assimilation model outperforms the simple statistical schemes at both tidal and nontidal frequencies (compare the last column of Table 1 with the Statistical Interpolation Errors columns). Comparing the four statistical hindcasts, no clear winner emerges: P3 gives the best fit to the tides, and the weighted average gives the best fit to the tidal residuals.

The improvement in the hindcast skill of the assimilation model over the four statistical schemes is illustrated in Figure 13. Although the weighted mean reproduces the northward tidal component at P1 reasonably well, it fails to capture the subtidal variability and the mean. By way of contrast, the assimilation model performs well at all frequencies. It also provides a smoother hindcast than the statistical schemes. One reason is the assimilation model is fit globally to all available data. Another reason is that both wind and barotropic submodels have local acceleration terms that make them act as low-pass filters. The statistical schemes, on the other hand, use only those observations available at a given time and so they are more sensitive to observation errors and changes in the distribution of the observing locations.

8. Summary

Observations made in spring 1991 and 1992 show the mean circulation over the crest of Western Bank is weak,

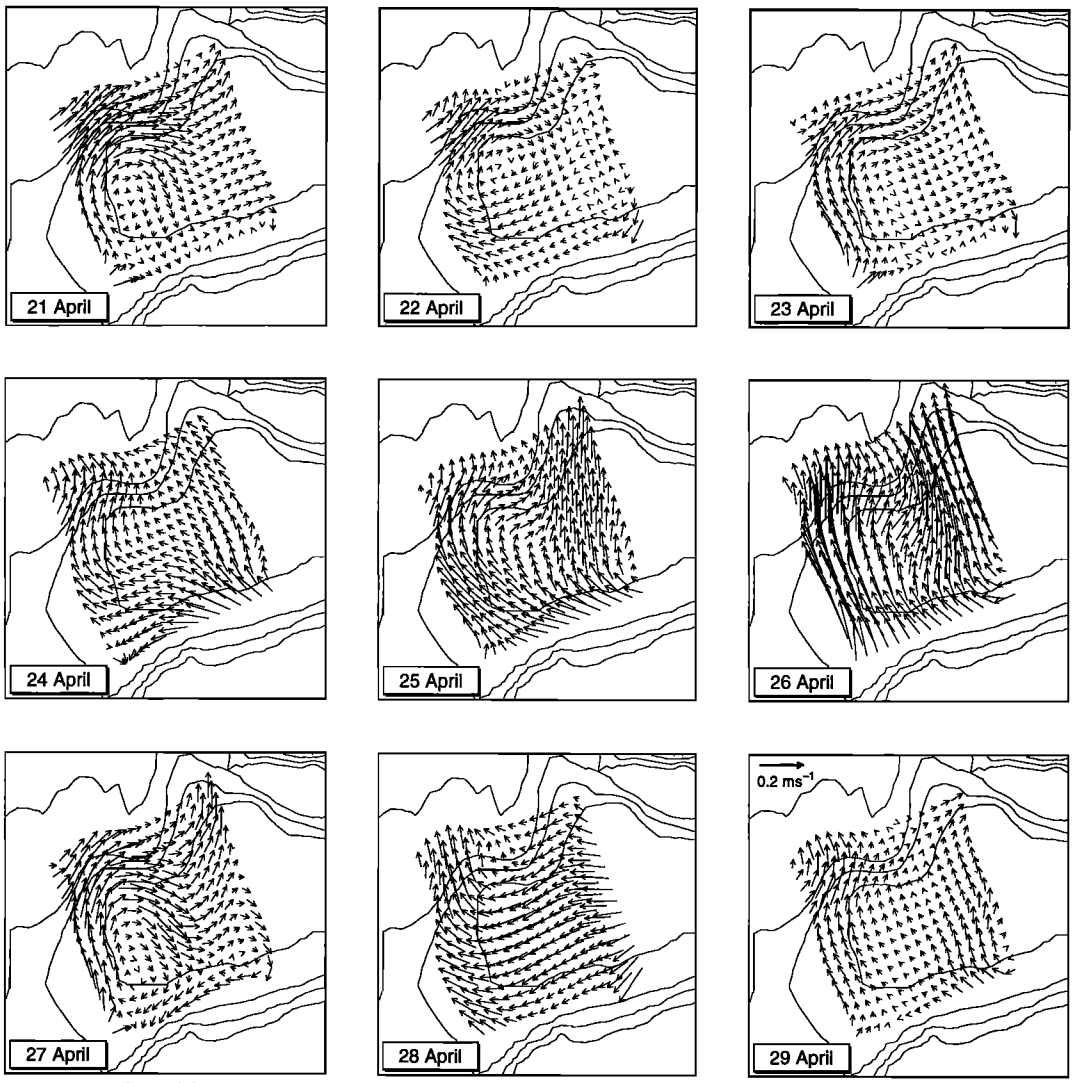

Figure 11. Subtidal flow fields from the assimilation model. (A 25-hour running mean, centered on noon of each day shown, was used to filter out the tides.) All available data were assimilated.

of the order of a few centimeters per second, and is flanked to the south and west by anticyclonic flows of about 10 cm s^{-1}. Thermal wind calculations show the mean circulation is due primarily to horizontal variations in the density field. It has been suggested recently [e.g., *Taggart et al.*, 1996; *McLaren and Avendaño*, 1995] that this circulation pattern and, in particular, the retention zone over the crest may be responsible for the high concentrations of chlorophyll, zooplankton, and cod eggs and larvae on Western Bank. This raises the possibility that strong winds may occasionally disrupt the gyre-like circulation and flush the bank of eggs and larvae, leading to high cod mortality and poor year-class strength. *Cong et al.* [1996] recently used a three-dimensional circulation model to test this idea. They calculated retention indices for Western Bank in spring and correlated them with the year-class strength of spring spawning cod over the period 1969 to 1990. The correlation, although weak, is different from zero at the 5% significance level, lending support to the idea that the gyre-like circulation on Western Bank is of biological importance.

Tides account for about three quarters of the current variance on Western Bank. The dominant M_2 constituent reaches speeds of 20 cm s^{-1}. The tidal residuals have a standard deviation of about 10 cm s^{-1}. Most of the residual energy is in the form of clockwise motions with a timescale of several days. Near-inertial peaks are evident in rotary spectra for some moorings on the flanks of the bank, but the peaks are shifted to frequencies below f. We attribute this to the influence of the anticyclonic background circulation on the effective inertial frequency. Correlations between the tidal residuals from different moorings are described reasonably well by functional forms derived from the theory of nondivergent, homogeneous, and isotropic turbulence. The characteristic length scale of these motions is 45 km. Statistical analysis and slab modeling show that local wind contributes to, but is not the main cause of, the residual variance.

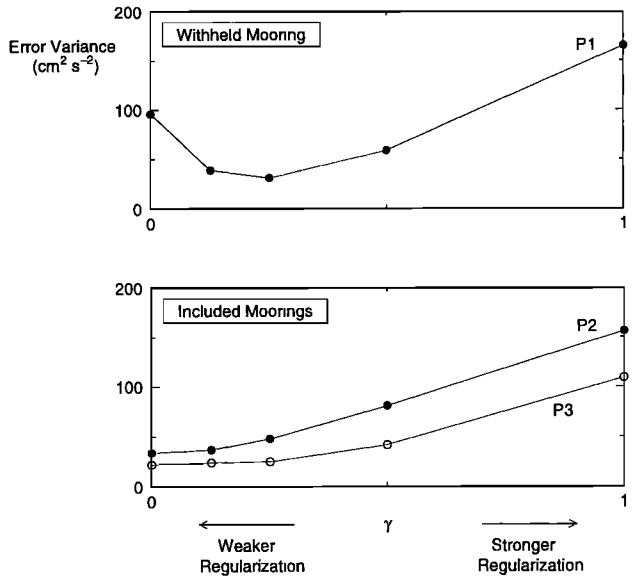

Figure 12. Error variance at the current moorings as a function of the regularization parameter γ. This parameter controls the size of the regularization terms J_b and J_v. Specifically, $\sigma_b = 4/3\gamma$ and $\sigma_v = 1/\gamma$, in (cm $s^{-1})^{-1}$. Thus large values of γ correspond to small values of σ_v and σ_b and hence strong regularization terms. (top) Error variance $(\sigma_u^2 + \sigma_v^2)$ at the mooring not included in the assimilation and (bottom) Error variance at moorings included in the assimilation.

To collect and interpret biological data from Western Bank, we needed an operational model to map its near-surface circulation. On the basis of the above description the flow was modeled as a linear combination of components driven separately by local wind, horizontal density gradients, and flows through the open boundaries of a limited-area barotropic model. Observations of bottom pressure, water density, and current were then assimilated into the model to infer the dynamic height field and open boundary conditions. Integrating the model over the cruise period then gave a dynamically consistent interpolation and extrapolation of the scattered observations over the whole model domain. One of the main conclusions of this study is that this approach produced better hindcasts than four simple statistical schemes. In other words the dynamics underlying the circulation model contributed useful information.

The assimilation scheme is based on exact enforcement of the dynamical constraints provided by the barotropic submodel. A more general approach is to allow system noise in the governing equations and infer it using the assimilation scheme (see appendix for details). We experimented with such an approach but found, not surprisingly, that the results were highly sensitive to the assumed covariance structure of the system noise. For the present application we therefore decided to take the simpler approach of assuming the barotropic dynamics to hold exactly. Note the baroclinic flow component allows some flexibility in fitting the barotropic model to the current observations. However, the baroclinic component is not arbitrary; the polynomials used in its specification ensure this flow component is large scale and it must also account for the variability in the observed dynamic heights.

Although we conclude data assimilation holds promise as a way of specifying open boundary conditions, it raises new problems for shelf modelers. To discuss these problems, it is convenient to formulate our assimilation scheme within the more familiar framework of multiple regression [e.g., *Thacker*, 1988b; *Wunsch*, 1996]. Following the development given in the appendix, the relationship between the observations and the unknowns

Table 1. Current Statistics for Mooring P1

	Observations	Statistical Interpolation Errors				Assimilation Error
		P2	P3	P2 + P3	Weighted	
Mean cm s^{-1}						
u	-0.9	-5.6	0.9	-2.3	-1.8	-1.8
v	-0.8	-9.8	-5.1	-7.5	-7.0	-0.3
Variance cm^2 s^{-2}						
Total	403	123	70	62	59	30
Tidal	299	38	14	19	17	8
Residual	104	85	56	43	42	22

Means and variances are given for the observations made from 0400 UT on April 21 to 1800 UT on May 1, 1992. Total variance refers to the sum of the variances of the east (u) and north (v) flow components. Tides were estimated by least-squares fitting a sum of sinusoids (M_2, S_2, O_1, and K_1) to the observations. Residuals were obtained by subtracting the tides from the observations, so the sum of the tidal and residual variance equals the total variance. Remaining data refer to errors made in hindcasting the flow at P1 using data from outside the data void (see Figure 8). P2, P3, and $\overline{P2 + P3}$ refer to interpolation schemes based on the observed currents at P2, P3, and their average, respectively. Weighted refers to the interpolation scheme in which observations from outside the data void are averaged, with a weighting factor that varies inversely as the third power of distance from P1. Assimilation errors are those made by the assimilation model, again using only data from outside the data void.

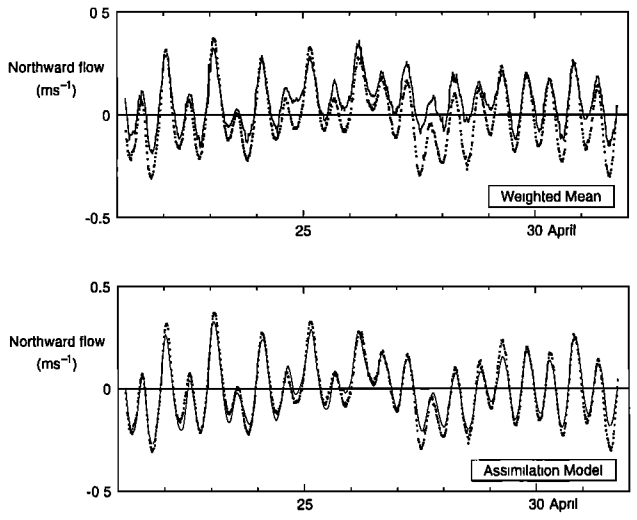

Figure 13. Observed and predicted northward flow at mooring P1, with dots denoting 15-min observations. Solid lines are (top) the weighted mean of all currents (moorings P2 and P3, the ADCP, and the drifters) measured outside the data void, with the weighting factor varying as r^{-3}, where r is distance from the center of the data void, and (bottom) the hindcast from the model that assimilates data from outside the data void.

of our linear model may be written $y = X\beta + \epsilon$, where y is the $n \times 1$ observation vector, β is the $p \times 1$ vector of unknowns, ϵ is the $n \times 1$ vector of errors, and X is a $n \times p$ transformation matrix that depends on the underlying dynamics and the observing array. We used generalized least squares to estimate β from y. The result is equivalent to choosing β to minimize a cost function which is a quadratic form in the unknowns. (For the type of problem of interest here, the minimization is carried out most efficiently using an adjoint model as explained in the appendix.) If the bottom friction parameter λ in the barotropic momentum equation had been treated as an unknown, or the advection term $\mathbf{u} \cdot \nabla \mathbf{u}$ added, the relationship between β and y would have to be generalized to a nonlinear model of the form $y = X(\beta) + \epsilon$.

In conventional shelf modeling the boundary conditions and other model unknowns are usually specified independently of interior observations. The model then is integrated over the period of interest and its performance assessed by comparing the predictions $X\beta$ against the independent observation y. In the present study the observations are used to estimate the unknowns. This leads to one of the questions raised in section 1: How does one assess the performance of the assimilation model given that it is driven by the observations? In principle, assessing the hindcast skill of the assimilation model is equivalent to assessing the fit of a multiple regression model to observations. In standard regression analysis the Hessian matrix is used to construct joint confidence regions for the true value of β. In the present application this is not practical because the Hessian matrix is so large (typically $10^3 \times 10^3$). Apart from examining the relative magnitudes of some of its off-diagonal to diagonal elements and calculating eigenvectors associated with extreme eigenvalues, the Hessian is difficult to handle. (We did calculate Hessians for some assimilation runs but chose, for the reasons given above, not to present them in this paper.) We used cross validation to assess model performance. A major difficulty with cross validation is choosing the validation data set. After some experimentation we decided to withhold observations made within a certain distance of the central mooring. Although such an approach is straightforward and of practical interest, it is somewhat arbitrary. Unfortunately, much of the statistical theory on cross validation is based on the assumption of independent and identically distributed errors. Such an assumption cannot be justified in the present situation, and so the theory is not particularly useful in choosing validation data sets. Hopefully, more experience with cross validation in the context of shelf modeling will lead to some accepted guidelines for assessing the hindcast skill of assimilation models.

The other question raised in section 1 relates to the relatively small number of observations n compared to the large number of unknowns p. Appending regularization terms to the cost function is equivalent to adding "bogus data" and therefore increasing n (see appendix). We chose the form of the regularization terms based on a combination of model sensitivity studies and physical intuition. Choosing their weights is not straightforward. Even for ridge regression, which corresponds to adding a regularization term of the form $\gamma\beta'\beta$ to the cost function, there remains controversy among statisticians concerning the choice of γ or if, indeed, ridge regression should be used at all [e.g., *Montgomery and Peck*, 1991]. We used cross validation to choose the weights of our regularization terms. It worked well, in that we were able to find weights that were clearly optimal and physically reasonable. The other way of improving the n to p ratio is to reduce p through model respecification. With a time step of 60 s and 16 inflow grid points along each boundary there are more than 10^6 potential boundary unknowns for the barotropic submodel. Allowing dynamic height to vary independently at each model time step and grid point increases the number of unknowns beyond 5×10^6. There is clearly a danger of overfitting the model to the observations. We used structure function expansions to control the number of unknowns. For example, with two structure functions for each open boundary and amplitudes specified every 3 hours, the number of unknown boundary inflows was reduced from about 10^6 to 182. The benefits of reducing p include faster convergence to the cost function minimum and flow fields that are less sensitive to model resolution.

There are several ways our assimilation scheme could be improved. Consider first the underlying dynamics. Although the linear decomposition of the flow

into three, separately modeled components was justified based on a statistical analysis of the available data for Western Bank, such a decomposition is not always valid. A straightforward extension of the present scheme would be to replace the slab and barotropic model by a single three-dimensional barotropic model forced by wind stress and boundary flows. This should lead to more realistic hindcasts of wind-driven currents and would allow current data from all depths to be assimilated. Perhaps the most important improvement would be to allow the density field and the mixing parameterizations to evolve with the flow. This would lead however to a cost function that is no longer a quadratic form in either the initial and boundary conditions. It may therefore have multiple minima and this could cause convergence problems for the assimilation scheme [e.g., *Tziperman, et al.*, 1992; *Marotzke and Wunsch*, 1993]. Additional difficulties would have to be faced in controlling baroclinic instabilities in the model, particularly for hindcasts longer than the growth time of the fastest growing mode.

The assimilation scheme could also be improved by assimilating more data. In the present study we assimilated drifter velocities rather than drifter trajectories. It would be interesting to attempt the latter, although the transformation $d\mathbf{x}/dt = \mathbf{u}(\mathbf{x}, t)$ would make the model nonlinear and again raise the possibility of a cost function with multiple minima. Coastal sea level is a readily available index of shelf circulation. To assimilate sea level from a number of coastal gauges, we have recently extended the model domain to include the whole of the Scotian Shelf, including the coastal boundary. The results of assimilating coastal sea level into a three-dimensional barotropic model with a diagnosed background baroclinic flow are encouraging and raise the possibility of a simple and effective operational model for nowcasting and forecasting the overall circulation of the region on timescales of days.

Appendix: Assimilation Scheme

This appendix provides technical details on the assimilation scheme. For readers unfamiliar with variational data assimilation it also provides an interpretation in terms of multiple regression. Adopting standard statistical notation, matrices (vectors) are denoted by upper (lower) case characters.

We first stack all observations in the vector y. In accord with the decomposition of the predicted flow into three components, we assume y is made up contributions from the local wind y_w, density gradients y_d, boundary flows y_b:

$$y = y_w + y_d + y_b + \epsilon. \tag{A1}$$

The last component ϵ is a zero-mean random error.

The wind contribution is calculated using (6) and does not involve parameter estimation.

The effect of water density on the surface flow and dynamic height, at any location and time, can be expressed as a linear combination of the d_{ks} using (7), (11), and (12). Therefore we can write

$$y_d = X_d d \tag{A2}$$

where d is the vector of stacked d_{ks} and X_d is a matrix that depends on the dynamical parameters f and g and when and where the observations were made.

Boundary-forced sea level and flow is found by integrating the shallow water equations using a scheme of the form

$$s_t = \tilde{D}_1 s_{t-1} + \tilde{D}_2 u_t \qquad t = 1, \ldots N \tag{A3}$$

where s_t is the model state vector (barotropic currents and sea levels at all interior grid points) and u_t is the corresponding vector of boundary flows at time t. $\tilde{D}_2$ includes the radiation conditions at the open boundaries. Efficient methods that take advantage of the sparseness of $\tilde{D}_1$ and $\tilde{D}_2$ are available to time step (A3).

If we start the integration from a state of rest (that is, $s_0 = 0$), the N state equations of (A3) can be stacked as follows

$$\begin{bmatrix} I & & & \\ -\tilde{D}_1 & I & & \\ & \ddots & \ddots & \\ & & -\tilde{D}_1 & I \end{bmatrix} \begin{bmatrix} s_1 \\ s_2 \\ \vdots \\ s_N \end{bmatrix} = \begin{bmatrix} \tilde{D}_2 & & & \\ & \tilde{D}_2 & & \\ & & \ddots & \\ & & & \tilde{D}_2 \end{bmatrix} \begin{bmatrix} u_1 \\ u_2 \\ \vdots \\ u_N \end{bmatrix} \tag{A4}$$

or equivalently,

$$D_1 s = D_2 u \tag{A5}$$

where $s = [s_1', \ldots s_N']'$, $u = [u_1', \ldots u_N']'$ and D_1 and D_2 are large, sparse matrices. The dimension of u is reduced by reexpressing the boundary flows as linear combinations of spatial structure functions (see (13) and (14)). Therefore we can write

$$u = Fb \tag{A6}$$

where b is the vector of stacked b_{ks} and F is made up of weights based on the ϕ_s and ω_k. The barotropic contribution to y is obtained by interpolation of s. Thus

$$y_b = Hs \tag{A7}$$

where H is a matrix of interpolation weights that depend on when and where the observations were made. Combining (A5) - (A7) gives

$$y_b = H D_1^{-1} D_2 F b \tag{A8}$$

or, more simply,

$$y_b = X_b b \tag{A9}$$

where

$$X_b = HD_1^{-1}D_2F. \tag{A10}$$

Combining these equations with (A1) and (A2) gives the following linear relationship between the wind corrected observations and the model unknowns:

$$y - y_w = X\beta + \epsilon \tag{A11}$$

where

$$X = [X_d \quad X_b] \tag{A12}$$

and

$$\beta = \begin{bmatrix} d \\ b \end{bmatrix} \tag{A13}$$

is the vector of unknowns to be estimated.

Let Σ denote the variance of ϵ. Generalized least squares then gives the following estimator for β

$$\hat{\beta} = (X'\Sigma^{-1}X)^{-1}X'\Sigma^{-1}(y - y_w) \tag{A14}$$

with error variance

$$\mathrm{Var}(\hat{\beta} - \beta) = (X'\Sigma^{-1}X)^{-1}. \tag{A15}$$

These equations also hold if we treat β as random [e.g., *Duncan and Horn*, 1972].

The Hessian matrix, $X'\Sigma^{-1}X$, was assumed nonsingular in deriving (A14). This assumption would be invalid if, for example, the number of unknown parameters exceeds the number of observations. For the present application the number of observations exceeds the number of unknowns but the Hessian is poorly conditioned. This leads to unstable estimates of β and unacceptably wide confidence intervals. (See *Thacker* [1988a, chapter 3] for a good discussion of the role of the Hessian in model fitting.) One way of overcoming this problem is through model respecification as in (A6). Another approach is to penalize unrealistic features in the model flow fields. This is equivalent to adding bogus data [e.g., *Thacker*, 1988b; *Harvey*, 1981]. To illustrate, let ζ_{ijt} denote the vorticity at grid point i, j and time t. Using (20), the vorticity can be expressed as a linear combination of the elements of s. Stacking all the ζ_{ijt} into the vector ζ, we can write

$$\zeta = Vs \tag{A16}$$

or equivalently,

$$\zeta = X_v b \tag{A17}$$

where

$$X_v = VD_1^{-1}D_2F. \tag{A18}$$

Assuming ζ to be a zero-mean random vector with covariance matrix Σ_v, (A11) may be augmented as follows

$$\begin{bmatrix} y - y_w \\ 0 \end{bmatrix} = \begin{bmatrix} X_d & X_b \\ 0 & X_v \end{bmatrix} \beta + \begin{bmatrix} \epsilon \\ \zeta \end{bmatrix}. \tag{A19}$$

Assuming ϵ and ζ are uncorrelated, generalized least squares gives the following modified estimator for β:

$$\hat{\beta} = (X'\Sigma^{-1}X + X_v'\Sigma_v^{-1}X_v)^{-1}X'\Sigma^{-1}(y - y_w). \tag{A20}$$

Thus, in principle, the estimation problem is solved. There is, however, a practical problem. The dimensions of the matrices in (A20) are too large to evaluate this expression directly. (For the application described in section 5 the dimension of D_1 is $14,544,800 \times 14,544,800$.) The problem is usually overcome [e.g., *Bennett*, 1992] by noting $\hat{\beta}$ minimizes the cost function

$$J(\beta) = \frac{1}{2}\epsilon'\Sigma^{-1}\epsilon + \frac{1}{2}\zeta'\Sigma_v^{-1}\zeta. \tag{A21}$$

The iterative scheme described in section 4 can then be used to minimize the cost function if its gradient with respect to the model unknowns is available for each iteration. Differentiating J with respect to d and b gives

$$\frac{\partial J}{\partial d} = -X_d'\Sigma^{-1}\epsilon \tag{A22}$$

$$\frac{\partial J}{\partial b} = (D_2F)'\lambda \tag{A23}$$

where

$$D_1'\lambda = -H'\Sigma^{-1}\epsilon + V'\Sigma_v^{-1}\zeta. \tag{A24}$$

The gradient of J with respect to d is straightforward to calculate following one model run to calculate $\Sigma^{-1}\epsilon$. The gradient of J with respect to b is calculated in two steps. First, λ is obtained from (A24) by running a model of the same form as (A3) backward in time (see (A4)), forcing it with the barotropic vorticity and the model errors:

$$\lambda_t = \tilde{D}_1'\lambda_{t+1} + f_t \qquad t = N, \ldots 1 \tag{A25}$$

where f_t is the appropriate subvector of $-H'\Sigma^{-1}\epsilon + V'\Sigma_v^{-1}\zeta$. The computational cost of calculating λ is about the same as one run of the barotropic model. The second step is to calculate $\partial J/\partial d$ from (A23). Equation (A25), the so-called backward or adjoint model, is usually derived using Lagrange multipliers in a constrained minimization of (A21). Details of that approach and references to previous work are given in GT.

The barotropic state vector s satisfies the discretized shallow water equations exactly. Adding noise to these equations ($s = D_1^{-1}D_2u + \eta$) presents no major difficulty and corresponds to replacing ϵ in the observation equation by $\epsilon + H\eta$. It does require, however, that the covariance of the noise η, Σ_η, be specified. The resulting $\hat{\beta}$ is equivalent to treating η as unknown and adding a term of the form $\eta'\Sigma_\eta^{-1}\eta$ to the cost function.

There are strong similarities between the approach outlined above and Kalman smoothing. For normally distributed variables the Kalman smoother minimizes a cost function of the form (A21) [e.g., *Jazwinski*, 1970,

section 5.3]. There are two reasons we did not use the Kalman smoother approach in this study. First, the dimension of our state vector is so large that the Kalman smoother is too computationally expensive. (*Webb* [1988] provides a good discussion of the practical problems that arise in oceanography when using the Kalman filter.) Second, although the barotropic submodel is first-order Markov as required by the Kalman smoother, the complete model is not because it includes a slowly evolving baroclinic component.

Acknowledgments. We first thank our colleagues at Dalhousie University, in particular, Jinyu Sheng and Dan Kelley for help with computing and graphics and Chris Taggart and Steve Lochmann for collecting data on Western Bank. Carlisle Thacker provided some useful hints that made our minimization routine more efficient and Mike Dowd kindly read and commented on the final draft of the manuscript. Finally we thank Gabe Csanady for sharing his deep insights on coastal processes and showing what can be done with simple models. This study was funded primarily by the Natural Sciences and Engineering Research Council of Canada through the Ocean Production Enhancement Network and the follow-on Interim Funding Research Programme and by IBM through its Environmental Research Program.

References

Abramowitz, M., and I. A. Stegun (Eds.), *Handbook of Mathematical Functions*, 1064 pp., Dover, Mineola, N. Y., 1965.

Allen, J. S., et al. Physical oceanography of continental shelves, *Rev. Geophys., 21*(5), 1149-1181, 1983.

Bennett, A. F., *Inverse Methods in Physical Oceanography, Cambridge Monogr. on Mech. and Appl. Math.*, 346 pp., Cambridge Univ. Press, New York, 1992.

Bretherton, F. P., R. E. Davis, and C. B. Fandry, A technique for objective analysis and design of oceanographic experiments applied to MODE-73, *Deep Sea Res., 23*, 559-582, 1976.

Brillinger, D. R., *Time Series Data Analysis and Theory*, 540 pp., Holden-Day, Merrifield, Va., 1981.

Cong, L., J. Sheng, and K. R. Thompson, A retrospective study of particle retention on the outer banks of the Scotian Shelf 1956-1993, *Can. Tech. Rep. of Hydrogr. and Ocean Sci., 170*, Bedford Inst. of Oceanogr., Dartmouth, N. S., 1996.

Csanady, G. T., The pressure field along the western margin of the North Atlantic, *J. Geophys. Res., 84*, 4905-4913, 1979.

Csanady, G.T., *Circulation in the Coastal Ocean*, 279 pp., D. Reidel, Norwell, Mass., 1982.

Daley, R., *Atmospheric Data Analysis*, 457 pp., Cambridge Univ. Press, New York, 1991.

D'Asaro, E. A., Upper-ocean inertial currents forced by a strong storm, III, Interaction of inertial currents and mesoscale eddies, *J. Phys. Oceanogr., 25*, 2953-2958, 1995.

Davies, A. M., Solution of the 3D linear hydrodynamic equations using an enhanced eigenfunction approach. *Int. J. Numer. Methods Fluids, 13*, 235-250, 1991.

Dowd, M., and K. R. Thompson, Extraction of tidal streams from a ship-borne acoustic Doppler current profiler using a statistical-dynamical model, *J. Geophys. Res., 101*, 8943-8956, 1996.

Duncan, D. B., and S. D. Horn, Linear dynamic recursive estimation from the viewpoint of regression analysis, *J. Am. Stat. Assoc., 67*(340), 815-821, 1972.

Fissel, D. B., and D. D. Lemon, Analysis of physical oceanographic data from the Labrador Shelf, summer 1980, *Contr. Rep. of Hydrogr. Ocean Sci., 39*, Bedford Inst. of Oceanogr., Dartmouth, N. S., 1991.

Ghil, M., and P. Malanotte-Rizzoli, Data assimilation in meteorology and oceanography. *Adv. Geophys., 33*, 141-265, 1991.

Gill P. E., W. Murray, and M. H. Wright, *Practical Optimization*, 401 pp., Academic, San Diego, Calif., 1981.

Griffin, D. A., and M. Cahill, *Dawson* cruises to Western Bank, February, April and December 1991, *OPEN Rep. 1993/2*, Dalhousie Univ., Halifax, N. S., 1993.

Griffin, D. A., and S. Lochmann, *Petrel V* cruise 22 to Western Bank, 17 April to 8 May, 1992, *OPEN Rep. 1992/6*, Dalhousie Univ., Halifax, N. S., 1992.

Griffin, D. A., and S. Lochmann, *Petrel V* cruise 31 to Western Bank, 22 November to 16 December, 1992, *OPEN Report 1993/1*, Dalhousie Univ., Halifax, N. S., 1993.

Griffin, D. A., and K. R. Thompson, The adjoint method of data assimilation used operationally for shelf circulation, *J. Geophys. Res., 101*, 3457-3477, 1996.

Harvey, A. C., *Time Series Models*, 229 pp., Philip Allan, Hertfordshire, England, 1981.

Heaps, N. S., On the numerical solution of the three dimensional hydrodynamical equations for tides and storm surges. *Mem. Soc. R. Sci. Liege, 6*(1), 143-180, 1972.

Helland-Hansen, B., The Sognefjord section, Oceanographic observations in the northern-most part of the North Sea and the southern part of the Norwegian Sea, in *James Johnstone Memorial Volume*, pp. 257-274, Lancashire Sea-Fisheries Laboratory, Univ. Press of Liverpool, Liverpool, 1934.

Jazwinski, A. H., *Stochastic Processes and Filtering Theory*, 376 pp., Academic, San Diego, Calif., 1970.

Lynch, D. R., and F. E. Werner, Three-dimensional hydrodynamics on finite elements, II, Linear time-stepping model, *Int. J. Numer. Methods Fluids, 7*, 507-533, 1991.

Marotzke, J., and C. Wunsch, Finding the steady state of a general circulation model through data assimilation: Application to the North Atlantic Ocean, *J. Geophys. Res., 98*, 20,149-20,167, 1993.

McLaren, I. A. and P. Avendaño, Prey field and diet of larval cod on Western Bank, Scotian Shelf, *Can. J. Fish. Aquat. Sci., 52*(3), 448-463, 1995.

Mellor, G. L., User's guide for a three-dimensional primitive equation, numerical ocean model, report, 35 pp., Program in Atmos. and Oceanogr. Sci., Princeton Univ., Princeton, N. J., 1992.

Montgomery, D. C., and E. A. Peck, *Introduction to Linear Regression Analysis*, 2nd. ed., 527 pp., Wiley-Interscience, New York, 1991.

Pedlosky, J., *Geophysical Fluid Dynamics*, 624 pp., Springer-Verlag, New York, 1979.

Pollard, R. T., and R. C. Millard, Comparison between observed and simulated wind-generated inertial oscillations, *Deep Sea Res., 17*, 813-821, 1970.

Schwing, F. B., Subtidal response of Scotian Shelf circulation to local and remote forcing, I, Observations, *J. Phys. Oceanogr., 22*, 523-541, 1992a.

Schwing, F. B., Subtidal response of Scotian Shelf circulation to local and remote forcing, II, Barotropic model, *J. Phys. Oceanogr., 22*, 542-563, 1992b.

Sheng, J., and K. R. Thompson, A robust diagnostic method for estimating surface circulation from vertical density profiles, *J. Geophys. Res., 101*, 25,647-25,659, 1996.

Taggart, C. T., S. L. Lochmann, D. A. Griffin, K. R. Thompson, and G. L. Maillet, Abundance distribution of larval

cod (*Gadus morhua*) and zooplankton in a gyre-like water mass on the Scotian Shelf, in *Survival Strategies in Early Life Strategies of Marine Resources*, edited by Y. Watanabe, Y. Yamashita, and Y. Oozeki, pp. 127-145, A. A. Balkema, Brookfield, Vt., 1996.

Thacker, W. C., Three Lectures on Fitting Numerical Models to Observations, Publ. GKSS 87/E/65, 64 pp., Forsch. Geesthacht GmbH, Phys. Inst. of GKSS, Geesthacht, Germany, 1988a.

Thacker, W. C., Fitting models to data by enforcing spatial and temporal smoothness, *J. Geophys. Res., 93*, 10,655-10,665, 1988b.

Tziperman, E., W. C. Thacker, R. B. Long, and S. M. Hwang, Oceanic data analysis using a general circulation model. I, Simulations, *J. Phys. Oceanogr., 22*, 1434-1457, 1992.

Webb, D. J., Assimilation of data into ocean models, in *Ocean Circulation Models: Combining Data and Dynamics*, NATO ASI Ser., Ser. C, Math. and Phys. Sci., vol. 284, pp. 233-256, edited by D. L. T. Anderson and J. Willebrand, Kluwer Acad., Norwell, Mass., 1988.

Wunsch, C., *The Ocean Circulation Inverse Problem*, 442 pp., Cambridge Univ. Press, New York, 1996.

D. A. Griffin, CSIRO Marine Research, Hobart, Tasmania, 7001, Australia.

K. R. Thompson, Department of Oceanography, Dalhousie University, Halifax, Nova Scotia, Canada B3H 4J1. (e-mail: Keith.Thompson@Dal.Ca)

(Received March 26, 1996; revised August 2, 1996; accepted December 18, 1997.)